Supporting Information for

Highly active PtFe alloy encapsulated in porous carbon fiber as air-cathode catalyst for zinc-air battery

Zhen An[a], Zizai Ma[b,c,*], Zihao Wan[a], Hongfei Xu[a], Jinping Li[c], Xiaoguang Wang[a,c,*]

[a] *Laboratory of Advanced Materials and Energy Electrochemistry, College of Material Science and Engineering, Taiyuan University of Technology, Taiyuan, 030024, China.*

[b] *College of Chemistry and Chemical Engineering, Taiyuan University of Technology, Taiyuan, 030024, China.*

[c] *Shanxi Key Laboratory of Gas Energy Efficient and Clean Utilization, Taiyuan University of Technology, Taiyuan, 030024, China.*

[*]*Corresponding Authors*

Email addresses: wangxiaoguang@tyut.edu.cn (X. Wang), mazizai@tyut.edu.cn (Z. Ma)

Experimental Section

Materials

All reagents and chemicals required for the experiment were directly utilized without additional treatment. Zinc nitrate hexahydrate ($Zn(NO_3)_2 \cdot 6H_2O$) and sodium hexachloroplatinate (IV) hexahydrate ($Na_2PtCl_6 \cdot 6H_2O$) were obtained from Sinopharm Chemical Reagent Co., Ltd. Iron nitrate nonahydrate ($Fe(NO_3)_3 \cdot 9H_2O$) and Polyacrylonitrile (PAN, Average Mw 250 000) were obtained from Shanghai Macklin Biochemical Co., Ltd. Pt/C (20 wt. %) was sourced from TANAKA and Nafion (5 wt. %) was sourced from Shanghai Hesen Electrical Co., Ltd.

Preparation of catalysts

Synthesis of PtFe-PAN fibers: PtFe-PAN was synthesized by electrospinning. 0.350 g PAN and 0.850 g $Zn(NO_3)_2 \cdot 6H_2O$ were dissolved in 7 mL DMF with magnetic stirring, then 0.058 g $Fe(NO_3)_3 \cdot 9H_2O$ and 0.072 g $Na_2PtCl_6 \cdot 6H_2O$ were added to the above solution at 50 °C in an oil bath and stirred until completely dissolved for subsequent electrospinning. The syringe tip was 18 cm from the drum-type collector, and the voltage was 15 kV. The flow rate was set at 0.001 mm/s^{-1} and the humidity was remained at 30%. A beige film was eventually deposited on the collector and dried overnight. The sample obtained was named as PtFe-PAN.

Synthesis of PtFe-PCF: PtFe-PAN was put to a ceramic boat and pre-

oxidized at 200 °C with the temperature ramp of 2°C min^{-1} under air atmosphere for about 2 hours, the sample was noted as PtFe-PAN@200. Then PtFe-PAN@200 was carbonized in an Ar atmosphere with a heating rate of 5 °C min^{-1} at 900 °C for 2 hours with a gas flow rate of 40 mL min^{-1}. The resultant product was labeled as PtFe-PCF.

Synthesis of the contrast catalysts: Pt-PCF, Fe-PCF, PtFe-CF were prepared by the same strategy without the addition of corresponding Fe, Pt and Zn sources. Moreover, PtFe-PC was obtained by direct pyrolysis of the electrospinning solution.

Physical characteristics

The morphology characteristics of catalysts were probed via Scanning Electron Microscopy (SEM, Hitachi S-4800). And Transmission Electron Microscopy (TEM, JEM-2100F) was employed to acquire the intricate microstructure and elemental distribution details. X-ray diffraction (XRD, DX-2700) employing Cu Kα radiation (40 kV, 30 mA, λ = 1.5406 Å) and X-ray Photoelectron Spectrometer (XPS, ESCALAB250XI) with Al Kα radiation (1486.68 eV) were employed to characterize crystal structure and the valence state of relevant elements of catalysts. Raman spectroscopy (HORIBA Scientific LabRAM HR Evolution) was conducted to analyze the degree of graphitization of the catalysts. An electrochemical Raman chamber, which was connected to a confocal Raman spectrometer, was utilized for in-situ electrochemical Raman measurement.

Electrochemical measurement

The electrochemical properties were examined in a three-electrode system by electrochemical workstation (Bio-Logic, VSP-3e). The glassy carbon electrode, the helical Pt wire electrode and and the saturated Ag/AgCl electrode were utilized as the working electrode, the counter electrode and the reference electrode, respectively. And the Nernst equation, which states that $E_{RHE} = E_{Ag/AgCl} + 0.197 + 0.059 \times pH$, was used to convert the saturated Ag/AgCl electrode into a reversible hydrogen electrode.

The catalyst ink is made in the following manner: 5 mg catalyst was dispersed into 300 μL isopropanol, 100 μL 0.5 wt. % Nafion and sonicated for 1h. Next, the rotating disk electrode (RDE, mass loading = 0.32 mg cm^{-2}) was used for electrochemical testing. The LSV curves at rotation speeds varying from 400 to 1600 rpm were accepted to analyze the number of electron transfers based on the Koutecky-Levich (K-L) equations as follows:

$$\frac{1}{j} = \frac{1}{j_K} + \frac{1}{j_D} = \frac{1}{j_K} + \frac{1}{B\omega^{1/2}} \quad (1)$$

$$B = 0.2nFC_0D_0^{2/3}\nu^{-1/6} \quad (2)$$

j, j_K and j_D stand for the measured current density, limiting diffusion current density and kinetic current density. ω and F correspond to the rotation speed of working electrode and the Faraday constant (F = 96485 C mol^{-1}),

C_0 and D_0 represent the saturation concentration of O_2 (1.2×10^{-3} mol L^{-1}) and the diffusion coefficient of O_2 (1.9×10^{-5} cm^2 s^{-1}). v denotes the kinematic viscosity of the electrolyte (0.01 cm^2 s^{-1}).

The rotating ring-disk electrode (RRDE, mass loading = 0.32 mg cm^{-2}) was utilized to measure the hydrogen peroxide yield (3) and electron transfer number (4). The formulas were used as follows:

$$H_2O_2(\%) = \frac{200Ir/N}{I_r/N + I_d} \quad (3)$$

$$n = \frac{4I_d}{I_r/N + I_d} \quad (4)$$

N denoted the current collection efficiency of the Pt ring electrode (N=0.37), I_d and I_r stood for the currents of disk electrode and ring electrode.

Assemble and evaluation of liquid-state zinc-air battery

The catalyst ink was produced by ultrasonic dispersion of 2.5 mg PtFe-PCF powder, 1 mg acetylene black, 4 mg carbon black into 200 μL isopropanol and 8 μL Nafion (5 wt. %). A polished zinc plate served as the anode, while the carbon fiber cloth coated with catalyst ink functioned as the cathode. The experiments on the zinc-air batteries were used an electrochemical workstation and LAND CT2001A in 6.0 M KOH as the electrolyte.

Assemble and evaluation of solid-state zinc-air battery

The solid electrolyte was fabricated as follows: 5g polyvinyl alcohol (PVA) was dissolved in 5 mL water by heating and magnetic stirring, and then 6.0 M KOH was introduced into the above solution in several times. The mixed solution was frozen to form a gel electrolyte. The test procedure is the same as for liquid zinc-air batteries.

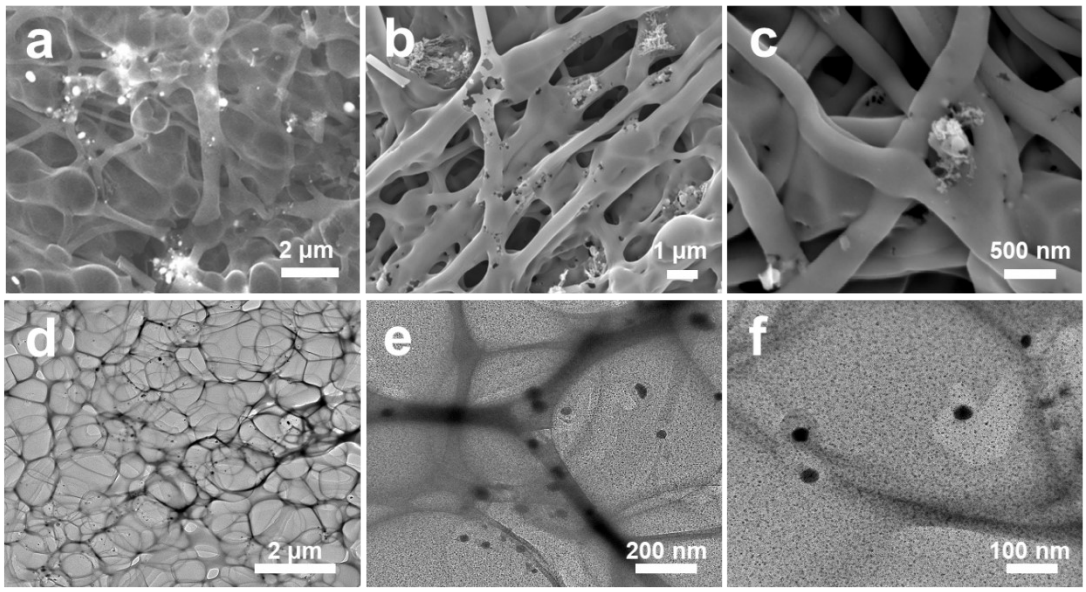

Figure S1. (a-c) SEM images of PtFe-PCF. (d-f) TEM and HRTEM images of PtFe-PCF.

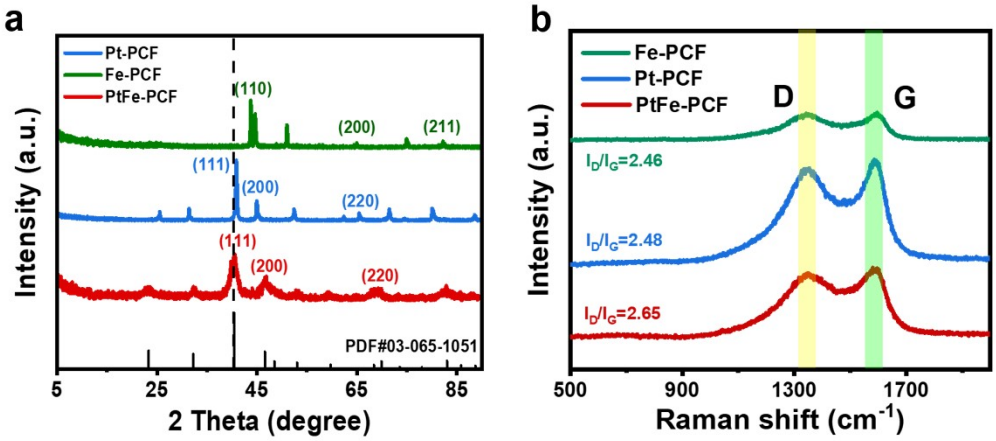

Figure S2. (a) XRD patterns and (b) Raman spectra of Fe-PCF, Pt-PCF and PtFe-PCF.

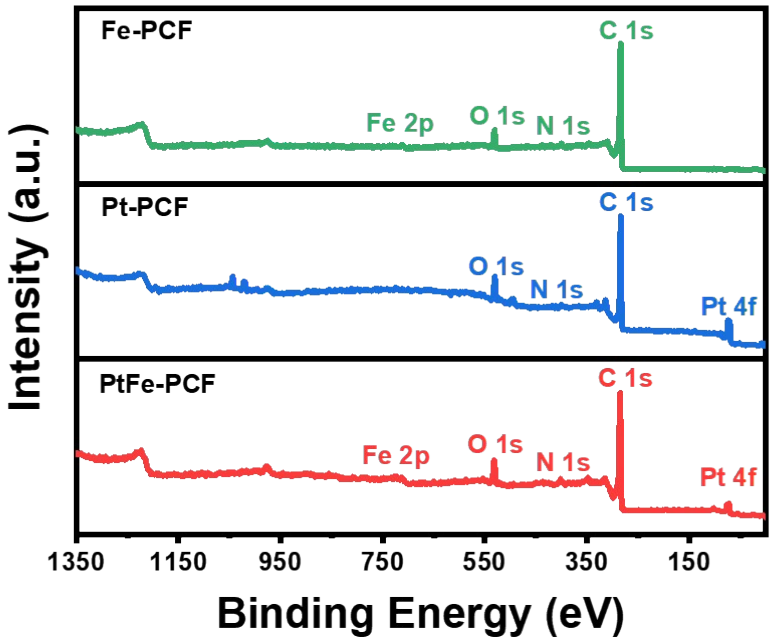

Figure S3. XPS full spectra survey of Fe-PCF, Pt-PCF and PtFe-PCF.

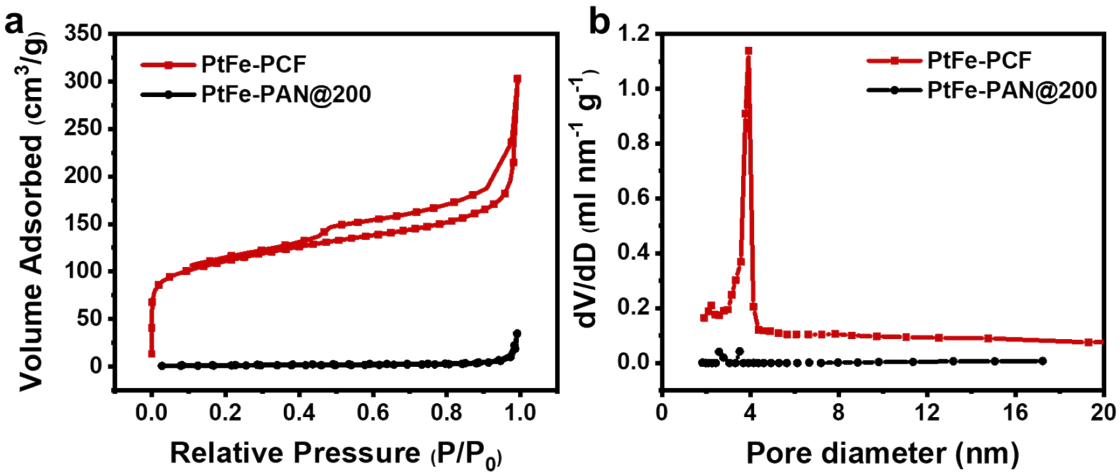

Figure S4. (a) N_2 adsorption and desorption isotherms and (b) pore size distribution curves of PtFe-PCF and PtFe-PAN.

The textural characteristics of fibrous samples--with (PtFe-PCF) and without (PtFe-PAN@200) high-temperature sintering--were systematically investigated through N_2 adsorption and desorption isotherms to quantify specific surface area and pore architecture (Figure S4). As shown in Figure S4a, PtFe-PCF exhibits a Type IV isotherm with a combined H_3/H_4-type hysteresis loop spanning P/P_0 =0.4-1.0, characteristic of mesoporous materials with slit-shaped or interconnected pore networks. The initial gradual adsorption at low relative pressures (P/P_0 <0.4) suggests monolayer-multilayer coverage, while the pronounced uptake at higher pressures (P/P_0 >0.4) correlates with capillary condensation in mesopores (2-4 nm) and secondary adsorption in larger, crack-like voids. In contrast, PtFe-PAN@200 displays a Type II isotherm with negligible hysteresis, consistent with non-porous or macroporous solids dominated by surface physisorption. Pore size distribution analysis (Figure S4b) confirms that PtFe-PCF possesses a narrow mesoporous regime (2-4 nm), whereas PtFe-PAN@200 lacks detectable porosity. Brunauer-Emmett-Teller (BET) calculations further reveal a striking disparity in specific surface area: PtFe-PCF achieves 361.6 m^2 g^{-1}, while PtFe-PAN@200 exhibits a minimal surface area of 4.1 m^2 g^{-1} (Table S3). This enhancement in PtFe-PCF's surface area is attributed to the evolution of hierarchical porosity-micropores and mesopores-driven by zinc volatilization during high-temperature sintering (900 °C).

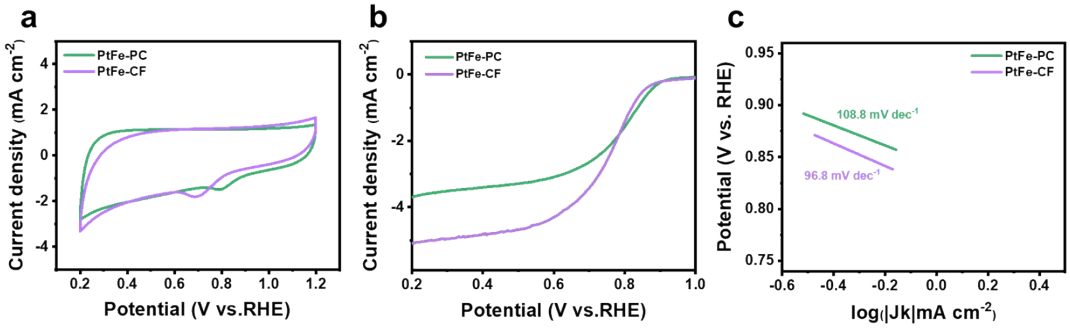

Figure S5. Electrocatalytic performance of the catalysts in O_2-saturated 0.1 M KOH. (a) CV curves, (b) LSV curves and (c) Tafel slopes of PtFe-PC and PtFe-CF.

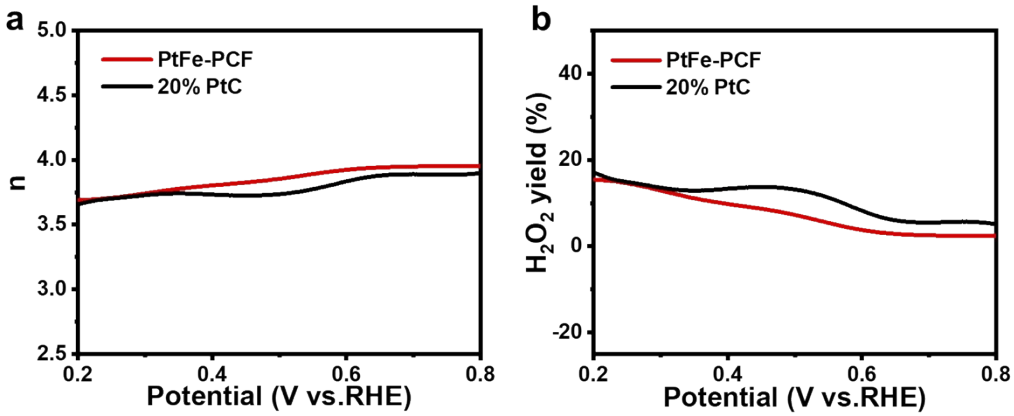

Figure S6. (a) Electron transfer number and (b) H_2O_2 yields of PtFe-PCF and 20%Pt/C in the potential range of 0.2-0.8 V vs. RHE in 0.1 M KOH.

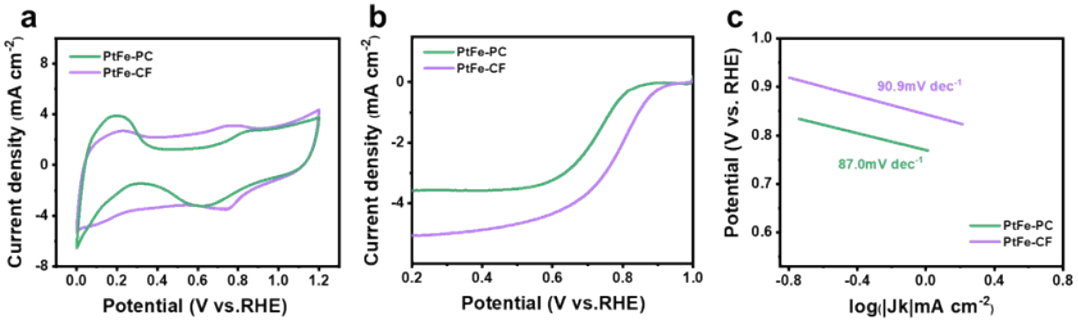

Figure S7. Electrocatalytic performance of the catalysts in O_2-saturated 0.1 M $HClO_4$. (a) CV curves, (b) LSV curves and (c) Tafel slopes of PtFe-PC and PtFe-CF.

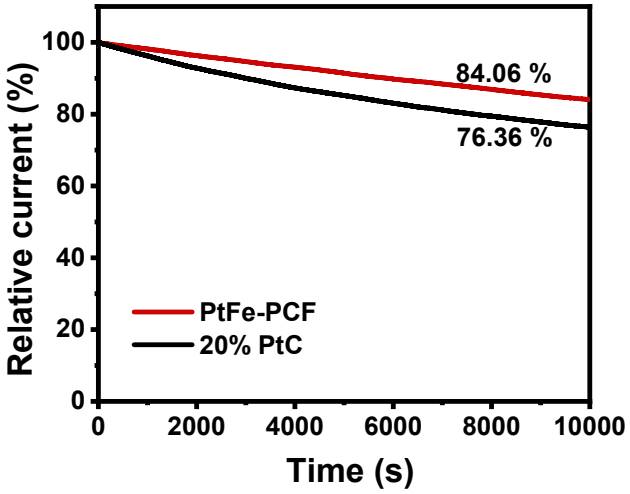

Figure S8. Long-term durability tests of 20% Pt/C and PtFe-PCF in 0.1 M $HClO_4$.

Table S1. The percentage of different N species in the N 1s of Fe-PCF, Pt-PCF and PtFe-PCF.

Sample	Pyridinic-N (wt. %)	Metallic-N (wt. %)	Pyrrolic-N (wt. %)	Graphite-N (wt. %)	Oxidized-N (wt. %)
Fe-PCF	16.3	7.5	35.9	20.3	19.9
Pt-PCF	20.6	7.6	35.5	9.9	26.5
PtFe-PCF	24.1	12.7	30.0	13.0	20.1

Table S2. The mass content of different elements in the XPS of PtFe-PCF.

Sample	C (wt. %)	N (wt. %)	O (wt. %)	Pt (wt. %)	Fe (wt. %)
Fe-PCF	75.0	4.3	10.0	6.8	3.8
Pt-PCF	70.2	2.9	15.0	11.9	—
PtFe-PCF	78.8	2.1	7.4	—	11.6

Table S3. Summary of specific surface area and pore characteristics of samples.

Catalysts	S_{BET}[a](m^2g^{-1})	Pore (nm)
PtFe-PCF	361.6	4.9
PtFe-PAN	4.1	—

Table S4. Comparison of the electrocatalyst PtFe-PCF performances of the prepared sample with reported Pt-based catalysts.

Catalyst	$E_{1/2}$ (V vs RHE)	Mass activity (mA mg_{Pt}^{-1})	References	Electrolyte
PtFe-PCF	0.853	573.9 at 0.85 V	This work	
Pt/d-CoP/NPC	0.820	153.0 at 0.80 V	[1]	
Pt-TNT/FAB	0.790	37.5 at 0.85 V	[2]	
Pt-SCFP/C-12	0.810	370.0 at 0.80 V	[3]	0.1 M KOH
Pt1@Pt/NBP	0.820	——	[4]	
Pt@Fe_{SA}-N-C	0.890	——	[5]	
PtFe-PCF	0.836	162.4 at 0.90 V	This work	
$Pt_{0.8}Ni_{0.2}$/C	0.810	390.1 at 0.90 V	[6]	
β-Ni(OH)2/Pt	0.840	740 at 0.90 V	[7]	
Pt1@Pt/NBP	0.867	214.0 at 0.90 V	[4]	0.1 M $HClO_4$
Ag@PtCo-rGO	0.864	450 at 0.90 V	[8]	
Pt@Fe_{SA}-N-C	0.850	510 at 0.90V	[5]	

Table S5. Comparison of kinetic current density (j_k) and mass activity of PtFe-PCF and 20% Pt/C.

	PtFe-PCF	20% PtC	Electrolyte
Loading for catalyst (mg cm^{-2})	0.0625	0.0625	
Loading for Pt (mg_{Pt} cm^{-2})	0.00425	0.0125	
J_k at 0.85V (mA cm^{-2})	2.439	1.880	
Mass activity at 0.85V (mA mg_{Pt}^{-1})	573.9	150.4	0.1 M KOH
J_k at 0.9V (mA cm^{-2})	0.831	0.816	
Mass activity at 0.9V (mA mg_{Pt}^{-1})	195.5	65.3	
J_k at 0.85V (mA cm^{-2})	2.286	1.381	
Mass activity at 0.85V (mA mg_{Pt}^{-1})	533.2	110.5	0.1 M $HClO_4$
J_k at 0.9V (mA cm^{-2})	0.690	0.408	
Mass activity at 0.9V (mA mg_{Pt}^{-1})	162.4	32.6	

Table S6. ICP data in electrolyte after 10000 cycles of catalysts in acid electrolyte.

Catalysts	Electrolyte	ICP (mg L^{-1}) Fe	ICP (mg L^{-1}) Pt
Fe-PCF	0.1 M $HClO_4$	0.65	/
Pt-PCF	0.1 M $HClO_4$	/	0.17
PtFe-PCF	0.1 M $HClO_4$	0.43	0.06

Table S7. Comparison of the performance of PtFe-PCF-based Zn-Air battery with other reported noble metal electrocatalysts.

Catalyst	Open-circuit voltage (V)	Maximum power density (mW cm^{-2})	Cycle Time (h) @J (mA cm^{-2})	Reference	Battery
PtFe-PCF	1.49	218.05	400 @5	This work	Liquid-state ZAB
Pt-NPs/CNR	1.46	165.4	42 @25	[9]	
FePc/FC	1.49	141	20 @10	[10]	
$Pt_{10}Fe_{12}Co_{15}Ni_{16}Mn_{27}Ga_{20}$/CNT	1.52	130.6	120 @5	[11]	
ZIF-67@Pt/CB	1.42	>150 m	50 @5	[12]	
Pt@Fe-MOF	1.397	104	95 @10	[13]	
Pt/HCMs	——	190	41 @10	[14]	
PtFe-PCF	1.51	128.63	14 @5	This work	Solid-state ZAB
Pt@Fe-MOF	——	49	20 @5	[13]	
PtFeCoNiMn/NC	1.41	192.16	95 @5	[15]	
PtPdFeCoNi/HOPNC	1.401	233.94	165 @10	[16]	
CC@FeCoNiMoRu-HEA/C	1.40	89.9	38 @2	[17]	
PAM-PAZn-Ss	——	61.08	62 @3	[18]	

References

[1] Z. Wu, Y. Gao, Z. Wang, W. Xiao, X. Wang, B. Li, Z. Li, X. Liu, T. Ma, L. Wang, Surface-enriched ultrafine Pt nanoparticles coupled with defective CoP as efficient trifunctional electrocatalyst for overall water splitting and flexible Zn-air battery, Chin. J. Catal. 46 (2023) 36-47.

[2] S. Bukka, R. Badam, R. Vedarajan, N. Matsumi, Photo-generation of ultra-small Pt nanoparticles on carbon-titanium dioxide nanotube composites: A novel strategy for efficient ORR activity with low Pt content, Int. J. Hydrogen Energy 44 (2019) 4745-4753.

[3] X. Wang, J. Sunarso, Q. Lu, Z. Zhou, J. Dai, D. Guan, W. Zhou, Z. Shao, High-Performance Platinum-Perovskite Composite Bifunctional Oxygen Electrocatalyst for Rechargeable Zn–Air Battery, Adv. Energy Mater. 10 (2020) 1903271.

[4] J. Liu, J. Bak, J. Roh, K.-S. Lee, A. Cho, J.W. Han, E. Cho, Reconstructing the Coordination Environment of Platinum Single-Atom Active Sites for Boosting Oxygen Reduction Reaction, ACS Catal.11 (2021) 466-475.

[5] F. Wang, X. Liu, B. Jiang, H. Zhuo, W. Chen, Y. Chen, X. Li, Low-loading Pt nanoparticles combined with the atomically dispersed FeN4 sites supported by FeSA-N-C for improved activity and stability towards oxygen reduction reaction/hydrogen evolution reaction in acid and alkaline media, J. Colloid Interface Sci. 635 (2023) 514-523.

[6] J. Liu, J. Lan, L. Yang, F. Wang, J. Yin, PtM (M = Fe, Co, Ni) Bimetallic Nanoclusters as Active, Methanol-Tolerant, and Stable Catalysts toward the Oxygen Reduction Reaction, ACS Sustainable Chem. Eng. 7 (2019) 6541-6549.

[7] X. Liu, S. Hao, G. Zheng, Z. Su, Y. Wang, Q. Wang, L. Lei, Y. He, X. Zhang, Ultrasmall Pt2Sr alloy nanoparticles as efficient bifunctional electrocatalysts for oxygen reduction and hydrogen evolution in acidic media, J. Energy Chem. 64 (2022) 315-322.

[8] X. Deng, S. Yin, Z. Xie, F. Gao, S. Jiang, X. Zhou, Synthesis of silver@platinum-cobalt nanoflower on reduced graphene oxide as an efficient catalyst for oxygen reduction reaction, Int. J. Hydrogen Energy 46 (2021) 17731-17740.

[9] A.K. Pradhan, S. Halder, C. Chakraborty, "Less is more": Carbon nanostructure-tailored low platinum containing electrocatalysts for improved zinc-air battery efficiency, J. Energy Storage 98 (2024) 113008.

[10] J. Chen, M. Wang, L. Chen, K. Guo, B. Liu, K. Wang, N. Li, L. Bao, X. Lu, Intrinsic Defect-Rich Carbon-Supported Iron Phthalocyanine as Beyond-Pt Oxygen Reduction Catalysts for Zinc–Air Batteries, Adv. Energy Sustain. Res. 5 (2024) 2400010.

[11] L. Luo, R. Tang, L. Su, J. Kou, X. Guo, Y. Li, X. Cao, J. Cui, S. Gong, Data-driven designed low Pt loading PtFeCoNiMnGa nano high entropy alloy with high catalytic activity for Zn-air batteries, Energy Stor. Mater. 72 (2024) 103773.

[12] J. Li, Z. Meng, D.J.L. Brett, P.R. Shearing, N.T. Skipper, I.P. Parkin, S. Gadipelli, High-Performance Zinc–Air Batteries with Scalable Metal–Organic Frameworks and Platinum Carbon Black Bifunctional Catalysts, ACS Appl. Mater. Interfaces 12 (2020) 42696-42703.

[13] C.-P. Wang, X. Lian, Y.-X. Lin, L. Cui, C.-N. Li, N. Li, A.-N. Zhang, J. Yin, J. Kang, J. Zhu, X.-H. Bu, Ultrafine Pt Nanoparticles Anchored on 2D Metal−Organic Frameworks as Multifunctional Electrocatalysts for Water Electrolysis and Zinc–Air Batteries, Small 19 (2023) 2305201.

[14] Z. Wang, D. Cheng, C. Chen, K. Zhou, Hierarchically porous carbon microspheres with fully open

and interconnected super-macropores for air cathodes of Zn-Air batteries, Carbon 136 (2018) 54-62.
[15] M. Xie, X. Xiao, D. Wu, C. Zhen, C. Wu, W. Wang, H. Nian, F. Li, M.D. Gu, Q. Xu, MOF-mediated synthesis of novel PtFeCoNiMn high-entropy nano-alloy as bifunctional oxygen electrocatalysts for zinc-air battery, Nano Res. 17 (2024) 5288-5297.
[16] M. Xie, Y. Lu, X. Xiao, D. Wu, B. Shao, H. Nian, C. Wu, W. Wang, J. Gu, S. Han, M. Gu, Q. Xu, Spatially Immobilized PtPdFeCoNi as an Excellent Bifunctional Oxygen Electrocatalyst for Zinc–Air Battery, Adv. Funct. Mater. n/a (2024) 2414537.
[17] Z. Hu, Q. Geng, S. Dong, M. Wang, Y. Song, W. Sun, H. Diao, D. Yuan, MOF-derived low Ru-loaded high entropy alloy as an efficient and durable self-supporting electrode in rechargeable liquid/flexible Zn-air batteries, J. Colloid Interface Sci. 671 (2024) 34-45.
[18] W. Zheng, Y. Zhao, H. Zhang, L. Zhang, Z. Zhang, Extending the Cycle Lifetime of Solid-State Zinc-Air Batteries by Arranging Stable Zinc Species Channels, ACS Appl. Mater. Interfaces. 16 (2024) 8885-8894.